Research Square

Preprints are preliminary reports that have not undergone peer review.
They should not be considered conclusive, used to inform clinical practice,
or referenced by the media as validated information.

Weakening Boundary Layer-Lower-Free-Troposphere coupling limits ENSO Amplification under Global Warming

Jae-Yeong Lee
Seoul National University
Geon-Il Kim
gikim8@gmail.com

Chosun University
Daehyun Kim
Seoul National University
Jong-Seong Kug
Seoul National University

Article

Keywords:

Posted Date: August 12th, 2026

DOI: https://doi.org/10.21203/rs.3.rs-10574165/v1

License: This work is licensed under a Creative Commons Attribution 4.0 International License.
Read Full License

Additional Declarations: No competing interests reported.

Weakening Boundary Layer-Lower-Free-Troposphere coupling limits ENSO Amplification under Global Warming

Jae-Yeong Lee[1], Geon-Il Kim[2*], Daehyun Kim[1], Jong-Seong Kug[1*]

[1]School of Earth and Environmental Sciences, Seoul National University, Seoul, South Korea

[2]Department of Environmental Engineering, Chosun University, Gwangju, South Korea

*Corresponding authors: Jong-Seong Kug (jskug1@gmail.com), Geon-Il Kim (gikim8@gmail.com)

Abstract

How ENSO-related atmospheric feedbacks respond to greenhouse warming remains uncertain. Using 31 CMIP6 models, we examine how future climate conditions alter the vertical structure of ENSO-related zonal winds and their transmission to surface wind stress. The multi-model mean shows that the 850-hPa zonal-wind response to Niño 3.4 sea surface temperature (SST) anomalies strengthens by about 29% in 2070–2100 relative to 1970–2000, whereas the zonal wind-stress response increases by only about 10%. This contrast reflects weakened coupling between the lower-free-troposphere and the boundary layer. We find that models with greater mid-tropospheric moistening exhibit an upward-shifted ENSO-related ascent profile, which weakens the projection of lower-free-tropospheric wind anomalies onto the boundary layer. Wind-stress decomposition further indicates that weakening of this coupling offsets about 8% of the projected enhancement. These results identify vertical atmospheric decoupling as a damping pathway that limits amplification of ENSO-related surface wind-stress feedbacks under global warming.

The El Niño-Southern Oscillation (ENSO) is the dominant mode of interannual climate variability , driven by coupled ocean-atmosphere interactions in the tropical Pacific[1,2]. Through atmospheric and oceanic teleconnections, ENSO exerts its influence far beyond the tropical Pacific, modulating large-scale circulation patterns across the globe[3,4]. These remote effects include precipitation anomalies and droughts[5], shifts in surface temperature[6], and substantial and persistent socioeconomic losses[7]. Extreme events may also trigger long-lasting reorganizations of regional climate regimes[8]. Despite its global impacts, accurately predicting and projecting ENSO's amplitude and periodicity remains challenging due to the complexity of the coupled ocean-atmosphere feedbacks that govern its evolution[1,9]. How ENSO variability will respond to increasing greenhouse gas concentrations remains one of a major uncertainty in climate science[10–12].

One major effort toward understanding future ENSO uncertainty has focused on identifying how the coupled feedback processes governing ENSO are altered under greenhouse warming[13–17]. Previous studies have primarily emphasized oceanic controls, highlighting the role of enhanced upper-ocean stratification, thermocline feedback changes, and subsurface ocean dynamics in modulating future ENSO variability[10,15,18]. Differences in these simulated oceanic processes are also considered an important source of inter-model uncertainty in future ENSO projections[19,20]. However, ENSO fundamentally arises from coupled ocean-atmosphere interactions, implying that changes in atmospheric feedback processes are just as important as oceanic processes in determining the overall strength of ENSO coupling. Atmospheric responses determine how SST anomalies generate surface wind stress, thereby directly influencing the efficiency of the Bjerknes feedback[3,21,22].

Recent studies highlight that greenhouse warming fundamentally alters the

thermodynamic structure of the tropical atmosphere, characterized by enhanced upper-tropospheric warming and increased tropospheric moisture[23,24]. While the role of atmospheric processes in modulating future ENSO amplitude has been widely acknowledged[25], the dynamical implications of these warming-induced thermodynamic shifts for ENSO atmospheric feedbacks are not fully understood. Because ENSO feedbacks are fundamentally mediated through tropical convective and circulation responses to SST variations, shifts in the vertical thermodynamic structure of the atmosphere may substantially alter how ENSO-related diabatic heating generates large-scale circulation anomalies. However, how these thermodynamic changes alter the vertical coupling among convective heating, atmospheric wind responses, and surface wind stress—and thereby affect ENSO strength—remains unclear.

In this study, we examine the atmospheric dynamical processes governing the ENSO-driven atmospheric response under future climate conditions. We find a robust weakening of vertical coupling across models, whereby the free-tropospheric wind response to sea surface temperature anomaly (SSTA) strengthens under future warming while the surface wind stress response fails to increase commensurately. Here, we refer to this relative weakening of vertical coupling as boundary-layer–lower-free-troposphere decoupling. This decoupling is stronger in models that simulate greater increases in mid-tropospheric specific humidity, suggesting that moisture-related changes in the vertical structure of convection reduce the transmission of lower-free-tropospheric wind anomalies to the surface. By identifying this atmospheric pathway, we provide a mechanistic framework that complements ocean-centered explanations of future ENSO amplitude change and clarifies how coupled atmosphere-ocean feedbacks may evolve under greenhouse warming.

Results

Boundary Layer-Lower-Free-Troposphere Decoupling

We first characterize the projected decoupling between the atmospheric boundary layer and the lower free troposphere across 31 CMIP6 models and then investigate the physical mechanisms responsible for this change. To this end, we calculated ENSO amplitude as the standard deviation of the DJF Niño 3.4 Index with a 31-year moving window. The ENSO amplitude simulated by the 31 models exhibits a nonlinear evolutionary pattern over the 1970-2100 period (Figure 1a), where values are expressed as the percentage change relative to each model's initial state (1985 Niño 3.4 variability). Notably, the amplitude increases until the mid-21st century and then declines. These nonlinear trajectories are consistent with findings reported in several previous studies [13,15]. In the multi-model ensemble mean, ENSO amplitude for the window centered on 2085 shows a modest net increase of approximately 6.6% relative to 1985; however, individual model responses exhibit a substantial spread, ranging from −3.0% to 15.7%. This wide inter-model spread underscores the persistent uncertainty in projecting future ENSO amplitude[11,14] and motivates a closer examination of the underlying atmospheric and oceanic processes that govern these divergent responses.

To understand the future evolution of ENSO, it is essential to examine the structural changes in the atmospheric and oceanic fields associated with ENSO, as these shifts can directly feed back into and modulate the ENSO amplitude itself. We focus on these variations by performing a linear regression of atmospheric and oceanic variables onto the Niño 3.4 Index, an approach that isolates the ENSO-driven component of each field and allows us to track how its intensity and spatial structure are transformed under warming. We then calculate the difference in the regressed coefficient between the late twenty-first century (2070-2100) and

present day (1970-2000) periods. This difference, denoted by ΔX, is hereafter referred to as the future change. For each variable X, it is defined as follows:

$$\Delta X = X_{2070-2100} - X_{1970-2000}$$

Figure 1b presents the relationship between ΔU_{850} – the projected change in the El Niño-related 850 hPa zonal wind response over the Niño 4 region – and ΔENSO amplitude, defined as the change in the DJF Niño 3.4 standard deviation calculated over a 31-year moving window. The Niño 4 region was selected because it exhibits the most robust low-level wind fluctuations during ENSO events. In the multi-model ensemble mean, the 850 hPa zonal wind response to ENSO intensifies by approximately 29% under future warming, while the overall ENSO amplitude increases by only approximately 6.6%. This stark contrast between a robust atmospheric strengthening and a muted ENSO response is already apparent at the ensemble-mean level. Across individual models, however, changes in ENSO amplitude show no coherent relationship with the near-universal strengthening of the 850-hPa wind response ($r = -0.16$).

This lack of correlation is particularly noteworthy because, from the perspective of air-sea interaction, an enhanced atmospheric response is theoretically expected to further amplify the ocean response and thereby increase the ENSO growth rate. In principle, the low-level wind response acts as a common multiplicative factor that strengthens all positive feedback terms contributing to ENSO growth[21,22,26]. Although previous studies have implicitly assumed that a stronger atmospheric response leads to heightened oceanic forcing and, consequently, increased ENSO amplitude[14], our CMIP6 results indicate a mismatch within this expected causal chain under global warming. A key to resolving this apparent contradiction lies in recognizing that the ocean responds primarily to surface wind stress rather than lower-free-tropospheric winds. However, the transmission of atmospheric circulation anomalies to the

ocean surface is strongly modulated by boundary-layer processes, which can substantially attenuate the signal[27,28]. Under greenhouse warming, this atmosphere–ocean coupling pathway may weaken. Consequently, although the ENSO-related U_{850} response intensifies in the future, its transmission to the ocean surface becomes less efficient, resulting in a much weaker increase in surface wind stress.

To directly examine the degree to which the enhanced lower-free-tropospheric wind response is transmitted to the ocean surface through this transmission pathway, we analyzed the ENSO-regressed zonal wind stress (τ_x) pattern and its projected changes under SSP5-8.5. The MME mean reveals that while the 850 hPa zonal wind response intensifies by approximately 29% (inter-model range: 17.6%), the corresponding increase in τ_x amounts to only 9.3% (range: 10.7%) – a disparity that is consistent across nearly all individual models (Figure 1c). This pronounced attenuation indicates that the strengthened atmospheric signal in the lower free troposphere is substantially damped before reaching the ocean surface, with the two quantities responding to warming in a disproportionate manner. This disparity implies that atmosphere-ocean momentum transfer is considerably less efficient in the future climate than the lower-free-tropospheric response alone implies, thereby providing a possible explanation for the weak correspondence between ΔU_{850} and ENSO amplitude change identified in Figure 1b. To further characterize the spatial coherence of this attenuation, we next examine the horizontal distribution of the future changes across multiple atmospheric levels.

Figure 2 shows the multi-model ensemble mean of the future changes (Δ) in the atmospheric variables (U_{850}, U_{1000}, τ_x) regressed onto the Niño 3.4 index. The 850 hPa westerly response strengthens robustly across the central equatorial Pacific, particularly over the Niño 4 region. The corresponding enhancement is substantially weaker at 1000 hPa. The

surface wind stress response also exhibits a less spatially extensive strengthening over the central equatorial Pacific. This progressive weakening of wind response enhancement from the lower free troposphere toward the surface over the Niño 4 region suggests that 'Boundary Layer-Lower-Free-Troposphere Decoupling' — wherein the enhanced lower-free-tropospheric wind response fails to penetrate effectively to the ocean surface — is a consistent feature of future climate projections. In the following analysis, we focus primarily on the mechanisms responsible for the attenuated strengthening of the 1000 hPa wind response before addressing the additional damping effect inherent in the wind stress transformation.

To gain a more detailed understanding of the 'Boundary Layer-Lower-Free-Troposphere Decoupling', we analyzed the vertical profiles of the zonal wind response averaged over the Niño 4 region (Figure 3a). In the present-day climate, the atmospheric response to ENSO exhibits a prominent first-baroclinic structure, characterized by low-level westerlies and upper-level easterlies separated by a nodal point where the wind response changes sign. A striking feature in the future climate projections is the distinct upward shift of this nodal point, alongside a general intensification of the zonal wind response across much of the lower troposphere. However, this strengthening is highly altitude dependent. While the enhancement of the westerly response is concentrated in the free troposphere (above 850 hPa), the near-surface change at the 1000 hPa remains marginal. The upward shift of the nodal point reflects an upward-shifted ENSO-related circulation structure, with weaker projection of lower-free-tropospheric wind anomalies onto the boundary layer. Because these vertical shifts in the wind response are closely tied to changes in the vertical distribution of convective heating, we next investigate the atmospheric processes responsible for the growing contrast between the strong intensification at 850 hPa and the weak surface wind stress response.

Top-heavy convective structure under future warming

Building on the identification of the 'Boundary Layer-Lower-Free-Troposphere Decoupling' in the previous section, we now investigate the physical mechanisms underlying this phenomenon. We first examine whether the vertical structure of ENSO-induced ascent changes under future warming, as such a shift can alter how the atmospheric wind response projects onto the boundary layer and lower free troposphere. To compare the vertical structure across models and climate states, we use normalized vertical profiles of the omega response to ENSO SSTA over the Niño 4 region (Figure 3b). Each profile is normalized by the magnitude of its peak upward-motion response, allowing us to focus on changes in the vertical distribution of the response rather than differences in its absolute magnitude. In the present-day climate, the Niño 4 region, a key area for deep convection during El Niño, exhibits a broad maximum in upward motion in the mid-troposphere. In the future climate, however, the peak of the omega response shifts upward, while the relative amplitude of ascent in the lower troposphere weakens. Because vertical motion in the tropical lower free troposphere is closely constrained by diabatic heating through the balance between diabatic warming and adiabatic cooling[29,30], this upward displacement of the omega profile is consistent with a more top-heavy diabatic heating structure. Such a vertical reorganization can concentrate the ENSO-induced wind response more strongly above the boundary layer while reducing its projection onto the boundary layer, providing a physical basis for the enhanced U_{850} response and the muted surface wind stress response identified in the previous section.

To explore the thermodynamic pathway associated with the upward shift of the ascent profile, we next examine the vertical profiles of specific humidity (q) and relative humidity (RH) over the Niño 4 region (Figure 3c, d). In the future climate, q increases throughout the

troposphere, indicating a broad increase in the absolute moisture content of the atmosphere. This increase is consistent with Clausius–Clapeyron scaling, under which saturation specific humidity increases with temperature if relative humidity does not decrease substantially[24]. Thus, part of the increase in q can be interpreted as a direct thermodynamic consequence of tropospheric warming. A related warming-driven mechanism is the upward displacement of the freezing or melting level, which can shift microphysical phase-change processes and the associated diabatic-heating structure toward higher altitudes, thereby contributing to a more top-heavy convective profile[31].

However, q alone does not indicate whether the free troposphere becomes moister relative to saturation. The RH profile addresses this point and shows a distinct increase in the mid-troposphere. This feature is consistent with previous studies that have attributed tropical mid-tropospheric moistening under warming to changes in last-saturation history and moisture transport pathways, including nonlocal thermodynamic control and circulation-driven increases in the transport of air whose last saturation occurred locally or nearby[32,33]. Such enhanced mid-tropospheric moisture can reduce entrainment-driven dilution of convective updrafts, thereby helping to maintain parcel buoyancy in the free troposphere and promoting deeper convection. This environment may favor an upward-shifted diabatic-heating profile, consistent with previous studies highlighting the critical role of mid-tropospheric humidity in regulating convective depth and organization[34–36]. Thus, the upward shift of the ascent structure may reflect both the background thermodynamic effects of warming, including melting-level rise, and the more direct convective influence of enhanced mid-tropospheric humidity.

If the upward shift of the ascent structure indeed weakens the dynamical linkage between the lower free troposphere and the boundary layer, such a change should be reflected

in a quantitative measure of vertical wind coupling. To test this idea, we define the Boundary Layer-Lower-Free-Troposphere Coupling Index (BFC index; I_{BFC}). I_{BFC} is calculated as the ratio of the ENSO-regressed zonal wind response at 1000 hPa to that at 850 hPa over the Niño 4 region, expressed as U_{1000}/U_{850}. This index measures the degree to which wind anomalies in the lower free troposphere are reflected near the surface. A larger I_{BFC} indicates stronger vertical coupling between the 850 hPa wind response and the 1000 hPa wind response, whereas a smaller index indicates weaker coupling between the lower free troposphere and the boundary layer. Thus, changes in I_{BFC} provide a diagnostic measure of whether the enhanced lower-free-tropospheric wind response under future warming is effectively transmitted downward to the near-surface atmosphere.

Figure 4a shows the projected changes in the I_{BFC} between the future and present climates across the 31 climate models. Out of the 31 models analyzed, 29 (approximately 93%) simulate a decrease in I_{BFC} under future warming, indicating a robust weakening of the vertical coupling between the boundary layer and the lower free troposphere. The consistency of this response across models provides strong support for the interpretation that future warming reduces the efficiency with which lower-free-tropospheric wind anomalies are transmitted to the surface. Despite this robust signal, the magnitude of the I_{BFC} reduction varies considerably among models (Figure 4a), suggesting that the strength of the decoupling depends on differences in the simulated thermodynamic and convective responses. This inter-model spread motivates further investigation into the physical factors controlling the I_{BFC} change.

To identify the physical factors controlling the inter-model spread in the I_{BFC} change, we examined the relationship between the BFC weakening, defined as $-\Delta I_{\mathrm{BFC}}$, and several

key variables over the Niño 4 region, including sea surface temperature (SST), precipitation, and mid-tropospheric q (Figure 4b). SST and precipitation show significant positive correlations with the BFC weakening (r = 0.56 and 0.51, respectively), indicating that stronger local warming and convective responses are associated with greater decoupling. However, the strongest relationship is found for mid-tropospheric q, which exhibits a substantially larger correlation (r = 0.71). Because changes in q reflect both the thermodynamic water-vapor increase associated with warming and additional moisture redistribution in the free troposphere, this result suggests that the combined effects of thermodynamic moistening and moisture redistribution in the mid-troposphere are most closely associated with the weakening of the I_{BFC}.

Because mid-tropospheric moisture emerges as the variable most strongly correlated with BFC weakening, we next examine whether this relationship depends on altitude. Figure 4c shows the vertical profile of $r\left(\Delta q(p), -\Delta I_{\mathrm{BFC}}\right)$, where $\Delta q(p)$ denotes the future change in specific humidity at each pressure level. The correlation is strongest between 400 and 700 hPa, indicating that moisture changes within the mid-troposphere are most closely associated with the future weakening of the boundary-layer–lower-free-troposphere coupling. Notably, this altitude range coincides with the layer exhibiting the largest increases in both q and RH (Figure 3c,d), suggesting that the enhanced mid-tropospheric moistening identified above is also the component most strongly linked to the inter-model spread in the BFC response.

To further examine how mid-tropospheric moistening is reflected in the vertical circulation structure, we performed a composite analysis by selecting the ten models with the largest increase in mid-tropospheric specific humidity (High-q group) and the ten models with the smallest increase (Low-q group) (Figure 5). The High-q group exhibits a distinctly more

top-heavy omega profile, with the maximum ENSO-induced ascent displaced toward the upper troposphere, whereas the Low-q group retains a broader mid-tropospheric maximum (Figure 5f, g). This difference in the vertical structure of ascent is accompanied by a clear contrast in the wind response. Although the High-q group shows a substantially larger projected increase in the 850 hPa westerly response, the corresponding enhancement at 1000 hPa is much weaker (Figure 5a, c), resulting in a reduced I_{BFC}. In contrast, the Low-q group exhibits a more vertically coherent wind response, allowing the lower-free-tropospheric wind anomalies to project more efficiently onto the boundary layer. The vertical profile of the zonal wind response further illustrates this difference, showing that stronger mid-tropospheric moistening is associated with enhanced wind anomalies above the boundary layer but comparatively limited strengthening near the surface (Figure 5e). Collectively, these composite results provide structural evidence that the stronger moistening within the mid-troposphere is accompanied by an upward reorganization of the ascent profile and a weakening of boundary layer–lower-free-troposphere coupling. While these composites illustrate the contrasting circulation structures associated with mid-tropospheric moistening, they compare only the opposite tails of the model distribution. We therefore next introduce a continuous metric that objectively quantifies the vertical displacement of the ascent profile across the full ensemble.

To quantify the vertical displacement of the ENSO-induced ascent profile, we defined the Center of Ascent (CoA), representing the pressure-weighted centroid of upward motion. This metric identifies the representative pressure level at which the ascent response is concentrated and provides an objective measure of the vertical position of the convective circulation. The CoA is calculated as

278 $$P_{CoA} = \frac{\sum_i(-\omega_i)p_i}{\sum_i(-\omega_i)}$$

279 where p_i denotes pressure and ω_i is the pressure velocity, and the summation is performed
280 only over ascending motion ($\omega < 0$). Lower values of P_{CoA} therefore indicate that the ascent
281 profile is centered at higher altitudes. Using this metric, we find that models with larger
282 increases in mid-tropospheric q exhibit more negative ΔP_{CoA} (Figure 6a), indicating that
283 enhanced moistening is associated with an upward displacement of the ascent centroid. This
284 relationship supports the composite results shown in Figure 5 by demonstrating that the linkage
285 between mid-tropospheric moistening and the vertical reorganization of the ascent profile holds
286 across the full ensemble of 31 climate models.

287 Furthermore, changes in P_{CoA} are positively correlated with changes in the BFC index
288 ($r = 0.58$; significant at the 99% confidence level), indicating that models with a larger upward
289 displacement of the ascent centroid also exhibit a greater weakening of boundary layer-lower-
290 free-troposphere coupling (Figure 6b). Together with the composite analysis, these
291 relationships consistently support the proposed mechanism whereby preferential mid-
292 tropospheric moistening is associated with an upward reorganization of the ENSO-induced
293 ascent profile, concentrating the atmospheric response higher in the free troposphere and
294 reducing its dynamical coupling to the boundary layer under future warming.

295

Impact of weakened vertical coupling on surface wind stress

The weakened vertical coupling helps explain why the substantially stronger 850-hPa wind response produces only a modest increase in surface wind stress. This process provides an atmospheric damping pathway that may limit ENSO amplification in a warmer climate. To quantify this effect, we focused on wind stress (τ), the primary mediator of air-sea interaction, and performed a diagnostic decomposition using the bulk formula. The perturbation of wind stress ($\Delta\tau'$) can be decomposed into contributions from the lower-free-tropospheric wind response (U'_{850}), the vertical coupling efficiency (I_{BFC}), and the background mean state as follows:

$$\frac{\Delta\tau'_x}{\tau'_x} \approx \frac{\Delta I_{BFC}}{I_{BFC}} + \frac{\Delta u'_{850}}{u'_{850}} + \frac{\Delta \bar{u}}{\bar{u}} + \epsilon$$

Our decomposition analysis reveals that while the U_{850} wind response generally intensifies in the future, this strengthening is partially offset by an approximately 8% negative contribution from BFC weakening (Fig. 7). Additionally, a reduction in the mean surface wind speed ($\overline{U}_{1000}$) serves as a further damping factor. Because surface wind stress depends nonlinearly on wind speed, a weaker background wind produces a smaller wind stress anomaly for the same ENSO-related wind perturbation. Together, these effects reduce the extent to which enhanced lower-free-tropospheric wind anomalies are translated into surface wind stress.

Discussion

In this study, we show that the CMIP6 models exhibit a robust divergence between the lower-free-tropospheric and near-surface atmospheric responses to ENSO under future warming. Although the ENSO-related zonal wind response strengthens substantially in the lower free troposphere, only a limited portion of this strengthening is reflected in the surface wind stress response. This contrast indicates that the strengthened free-tropospheric circulation response does not project proportionally onto the boundary layer and surface wind stress. Although the moderate increase in the surface wind stress response is consistent with a previous study[14], our results further suggest that changes in the vertical structure of the atmospheric response provide an important pathway for modulating ENSO-related wind feedbacks under greenhouse warming.

Our analysis points to mid-tropospheric moistening as a key factor associated with this vertical decoupling. Models with stronger increases in mid-tropospheric specific humidity tend to exhibit a larger upward-shift in the ENSO-induced ascent profile, as measured by the Center of Ascent. This upward reorganization is accompanied by a lower BFC index (I_{BFC}), indicating that lower-free-tropospheric wind anomalies are less efficiently projected onto the boundary layer. Rather than implying a direct one-way causal relationship, these results support a physically consistent pathway in which future thermodynamic and moisture changes favor an upward-shifted convective circulation structure, thereby weakening the near-surface expression of the strengthened free-tropospheric wind response.

This mechanism provides a dynamical complement to the conventional thermodynamic expectation that increased atmospheric moisture may enhance tropical convective heating and atmospheric feedbacks. Our results suggest that the vertical

organization of this enhanced convective response is equally important: while increased moisture can support stronger convection, the accompanying upward displacement of the ascent and heating structure can reduce the efficiency with which the atmospheric response is expressed at the surface. In this sense, boundary-layer–lower-free-troposphere decoupling acts as a damping pathway that may help limit the amplification of ENSO surface wind stress feedbacks in a warmer climate. Accounting for the vertical structure of atmospheric circulation, therefore, offers a more complete framework for understanding how ENSO feedbacks evolve under greenhouse warming.

The implications of this framework may extend beyond the tropical Pacific. Because mid-tropospheric moistening and the upward reorganization of vertical motion can alter how SST anomalies project onto near-surface wind responses, similar processes may also influence other tropical modes of variability, such as the Indian Ocean Dipole. Whether such boundary-layer–lower-free-troposphere decoupling operates in other basins remains an open question. Applying this framework beyond the Pacific could help clarify how tropical air–sea coupling changes under greenhouse warming.

Several limitations should be noted. First, our analysis relies on CMIP6 models, whose representations of convection, entrainment, and boundary-layer processes differ substantially across models. These differences may influence both the simulated vertical structure of ENSO-induced ascent and the strength of the inferred BFC weakening. Second, although the inter-model relationships among mid-tropospheric moistening, the Center of Ascent, and the BFC index support a coherent physical interpretation, they do not by themselves establish causality. Targeted process-level diagnostics, including diabatic heating profiles, convective mass flux, detrainment, and boundary-layer momentum budgets, would help further test the proposed

mechanism. Future studies using global storm-resolving models, convection-permitting simulations, or observational constraints on tropical boundary-layer coupling will be valuable for assessing the robustness of this decoupling pathway and reducing uncertainty in projections of ENSO atmospheric feedbacks.

Methods

Model outputs

To evaluate future climate change, we used simulation data from 31 Coupled Global Climate Models (CGCMs) participating in the Coupled Model Intercomparison Project phase 6 (CMIP6; Supplementary Table 1). We analyzed the historical simulations for 1970-2014 and the Shared Socio-economic Pathway 5-8.5 (SSP5-8.5) simulations for 2015-2100. Within each 31-year moving window, we removed the linear trend and calculated monthly anomalies relative to the corresponding window climatology. ENSO amplitude was defined as the standard deviation of December-January-February (DJF) Niño 3.4 index within each 31-year window.

Statistical significance test

To evaluate the statistical significance and estimate the uncertainty of our results, we applied the bootstrap method in the following ways. (1) Uncertainty of the multi-model ensemble (MME) mean. We carried out random sampling of the 31 models with replacement 10,000 times to determine the confidence intervals of the MME mean (Figs. 1a, 3a-d, 5e-f). (2) Significance of the inter-model correlation. To estimate the confidence intervals of the correlation coefficients across the models (e.g., between SST and I_{BFC} changes), we randomly sampled the paired data from the 31 models with replacement 10,000 times and recalculated the correlation coefficient for each iteration (Fig. 4b). For both methods, the 95% confidence intervals are defined by the 2.5th and 97.5th percentiles of the 10,000 bootstrapped samples.

Detecting the Center of Ascent

To quantify the vertical position of ENSO-related ascent, we define the Center of Ascent (P_{CoA}) as the pressure-weighted centroid of upward motion. This metric identifies the representative pressure level where vertical motion is most concentrated, allowing us to physically track the vertical displacement of the ascent profile. Since pressure decreases with altitude, a lower P_{CoA} value corresponds to a higher altitude of the convective center. Therefore, a decrease in P_{CoA} provides a measure of a transition toward a more top-heavy convective structure, whereas an increase signifies a bottom-heavy shift.

Our definition of P_{CoA} is conceptually analogous to the 'centroid of latent heating' widely used in tracking the vertical evolution of tropical convection[37,38]. While previous studies have often characterized convective structures using a 'Top-heaviness index'—typically derived from the ratio of baroclinic mode amplitudes via EOF decomposition[39,40]—we adopt an alternative approach better suited to our specific analytical framework. Because we analyze ω profiles regressed onto the Niño 3.4 index, the ENSO-driven signal is inherently isolated into a representative spatial structure. Since the temporal variability is already constrained by this linear regression, conducting further statistical mode decomposition is unnecessary. Instead, calculating P_{CoA} allows us to directly and physically quantify the vertical displacement of the convective 'center of mass' across the multi-model ensemble, thereby providing a more intuitive and continuous measure of the vertical shift in the atmospheric response to global warming.

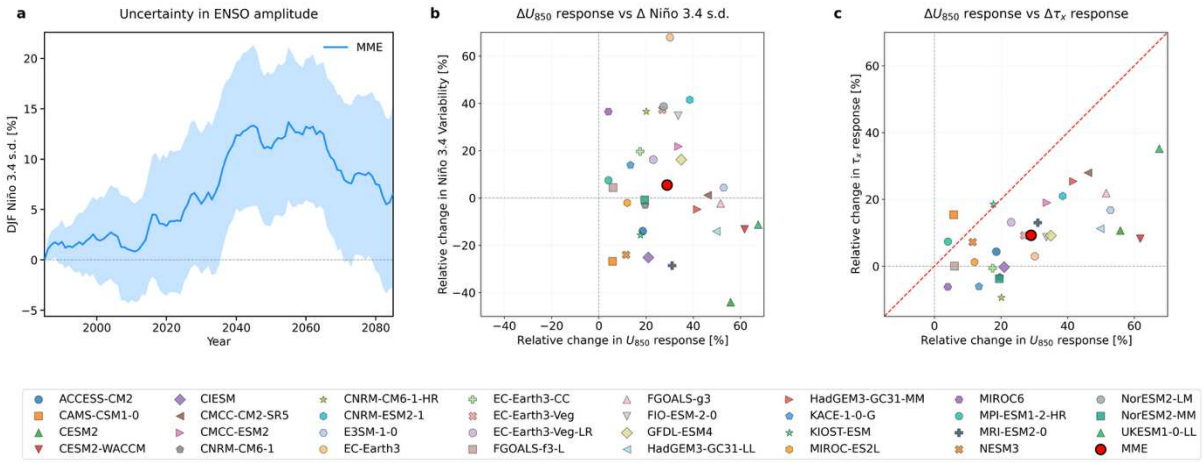


Figure 1. Inter-model variations in ENSO amplitude changes and the responses of lower-free-tropospheric wind and surface wind stress to ENSO under global warming

(a) Time series of the relative change (%) in the winter (DJF) Niño 3.4 index standard deviation (s.d.) from 1985 to 2085, compared to the 1985 baseline. The Niño index for a specific year was calculated by applying a 31-year moving window centered on that year to remove the climatology and linear trend. The solid blue line represents the CMIP6 Multi-Model Ensemble (MME) mean, and the shaded area of the same color indicates 95% bootstrap confidence interval of the multi-model mean. (b) A scatter plot across CMIP6 models showing the relative changes (%) – calculated by dividing the 2085 values by the 1985 baseline values – in the lower-free-tropospheric (850 hPa) zonal wind ($\mathbf{U_{850}}$) response to typical ENSO events versus the Niño 3.4 variability. The wind response is defined as the average zonal wind in the Niño 4 region regressed onto the Niño 3.4 index. Here, the markers represent individual CMIP6 models, and the large circle with a red outline indicates the MME. The specific models corresponding to each marker are listed below. (c) As in (b) but comparing the relative changes (%) in the $\mathbf{U_{850}}$ response to ENSO against the relative changes (%) in the sea surface zonal wind stress ($\boldsymbol{\tau_x}$) response to ENSO. The red dashed line denotes the 1:1 reference line (y=x). In (c), the predominance of models below the 1:1 reference line indicates that the relative increase in the $\boldsymbol{\tau_x}$ response is smaller than that in the $\mathbf{U_{850}}$ response.

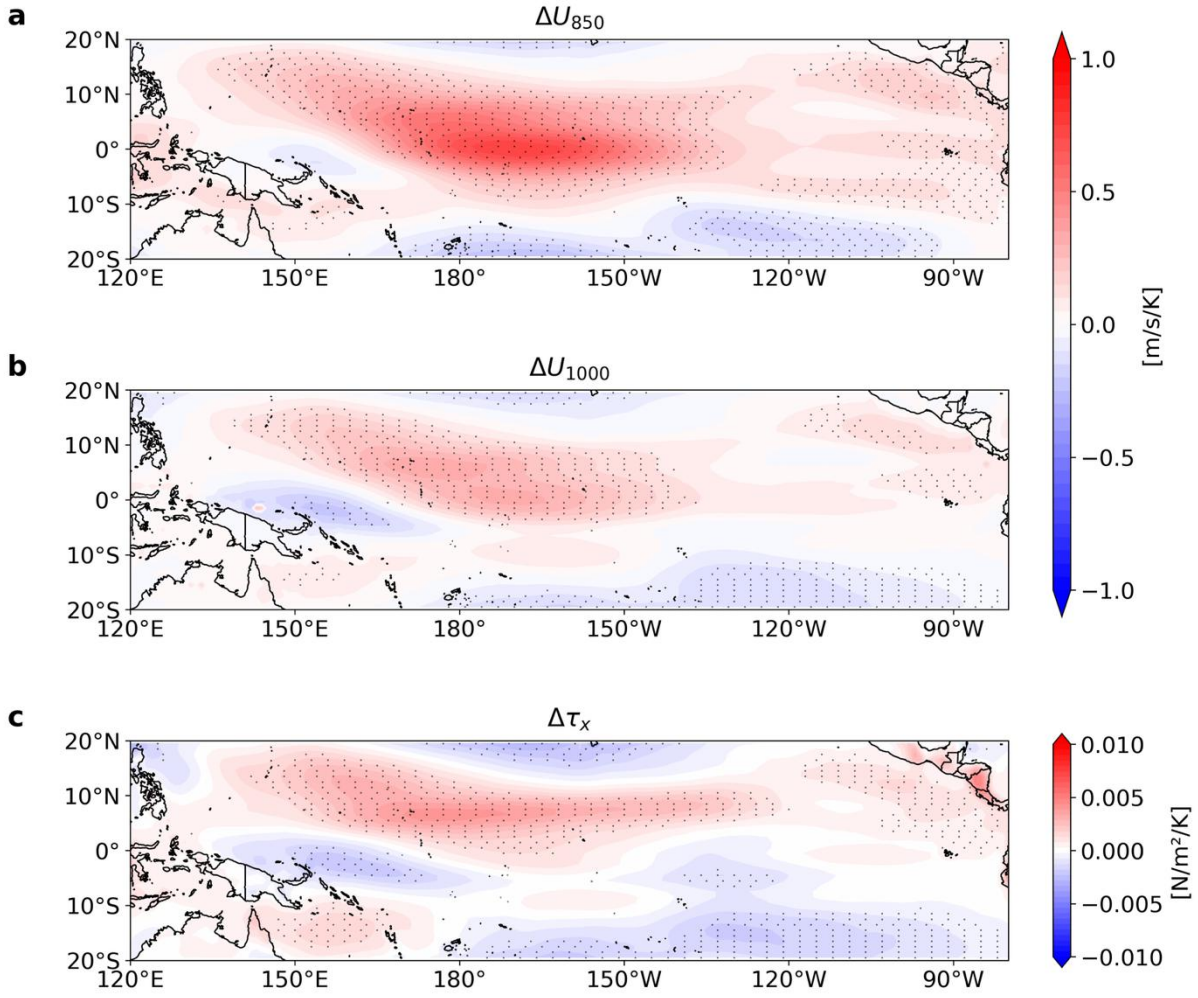


Figure 2. Projected changes in the spatial distribution of lower-free-tropospheric, near-surface wind and surface wind stress responses to El Niño

Spatial distributions of the differences in the responses to a 1K Niño 3.4 anomaly between the global warming (2070-2100) and present-day climates (1970-2000) for: (a) the lower-free-tropospheric (850 hPa) zonal wind response ($\mathbf{\Delta U_{850}}$, m/s/K), (b) the near-surface (1000 hPa) zonal wind response ($\mathbf{\Delta U_{1000}}$, m/s/K), and (c) the sea surface zonal wind stress response ($\mathbf{\Delta \tau_x}$, N/m²/K). Red (blue) shading indicates an intensification (weakening) of the westerly wind response. Stippling indicates grid points where the multi-model mean future-minus-present difference is significant at the 95% confidence level based on a paired t-test across models. In (a), a distinct intensification of the lower-free-tropospheric zonal wind response ($\mathbf{\Delta U_{850}}$) is observed across the central equatorial Pacific, particularly centered over the Niño 4 region. However, the response magnitudes of the near-surface wind ($\mathbf{\Delta U_{1000}}$) in (b) and the wind stress ($\mathbf{\Delta \tau_x}$) in (c) fall short of this level.

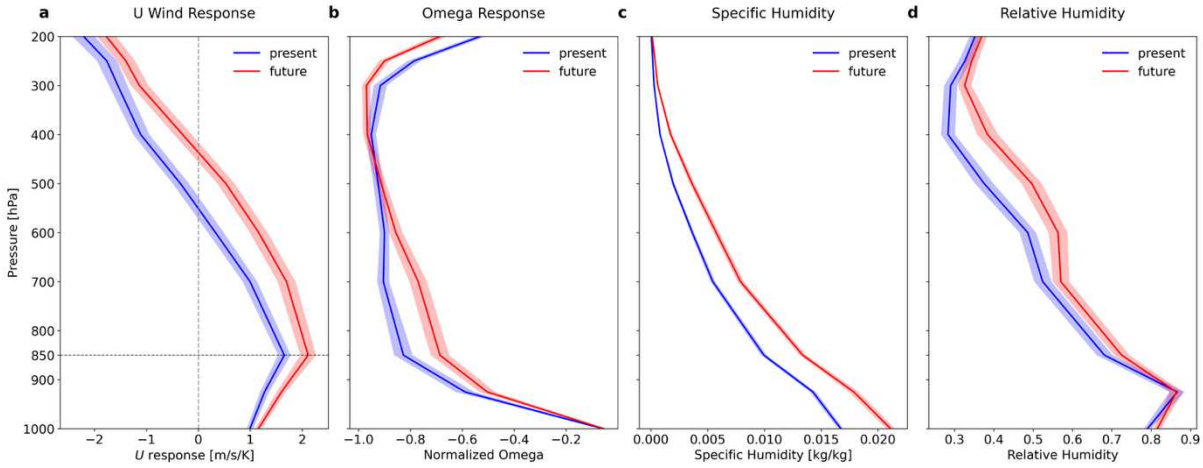


Figure 3. Projected changes in the vertical atmospheric response to El Niño and its link to climatological moisture profiles.

Vertical profiles (1000–200 hPa) over the Niño 4 region for: (a) the zonal wind response (U response, m/s/K), (b) the normalized pressure-velocity ($\boldsymbol{\omega}$) response, (c) climatological specific humidity (kg/kg), and (d) climatological relative humidity. The solid blue line represents the present-day climate (1970-2000), while the solid red line represents the future warming climate (2070-2100). The light shading around the solid lines indicates inter-model uncertainty (95% bootstrap range). The horizontal dotted line in panel (a) indicates the 850 hPa level which shows the strongest wind response. As shown in (c) and (d), specific humidity increases throughout the troposphere, whereas relative humidity increases primarily in the mid-troposphere.

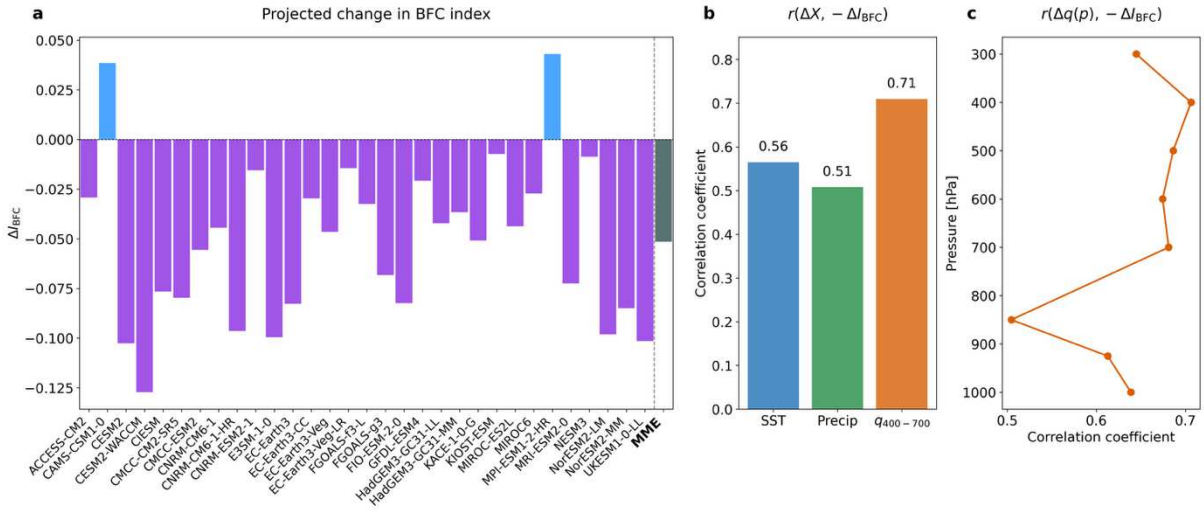


Figure 4. Inter-model spread of the Boundary-Layer-Lower-Free-Troposphere Coupling index and its relationship with future moisture changes.

(a) Projected future changes in the BFC index, ($\mathbf{I}_{\mathrm{BFC}} = \mathbf{U_{1000}/U_{850}}$), across 31 CMIP6 models and the multi-model ensemble mean (MME; gray bar). Here $\mathbf{U_{1000}}$ and $\mathbf{U_{850}}$ denote the ENSO-regressed zonal wind responses over the Niño 4 region. Negative $\Delta\mathbf{I}_{\mathrm{BFC}}$ indicates a weaker boundary-layer response relative to the lower-free-tropospheric response, corresponding to stronger decoupling. Among the 31 models, 29 show negative $\Delta\mathbf{I}_{\mathrm{BFC}}$. (b) Correlation coefficients between BFC weakening, defined as ($-\Delta\mathbf{I}_{\mathrm{BFC}}$), and projected changes in SST, precipitation, and layer-mean specific humidity between 400 and 700 hPa ($\Delta\boldsymbol{q_{400-700}}$), over the Niño 4 region. The strongest correlation is found for $\Delta\boldsymbol{q_{400-700}}$ (r = 0.71). (c) Vertical profile of the correlation coefficient $\boldsymbol{r(\Delta q(p), -\Delta I_{BFC})}$, where $\Delta\boldsymbol{q(p)}$ denotes the future change in specific humidity at each pressure level. The correlation peaks in the mid-troposphere, approximately between 400 and 700 hPa.

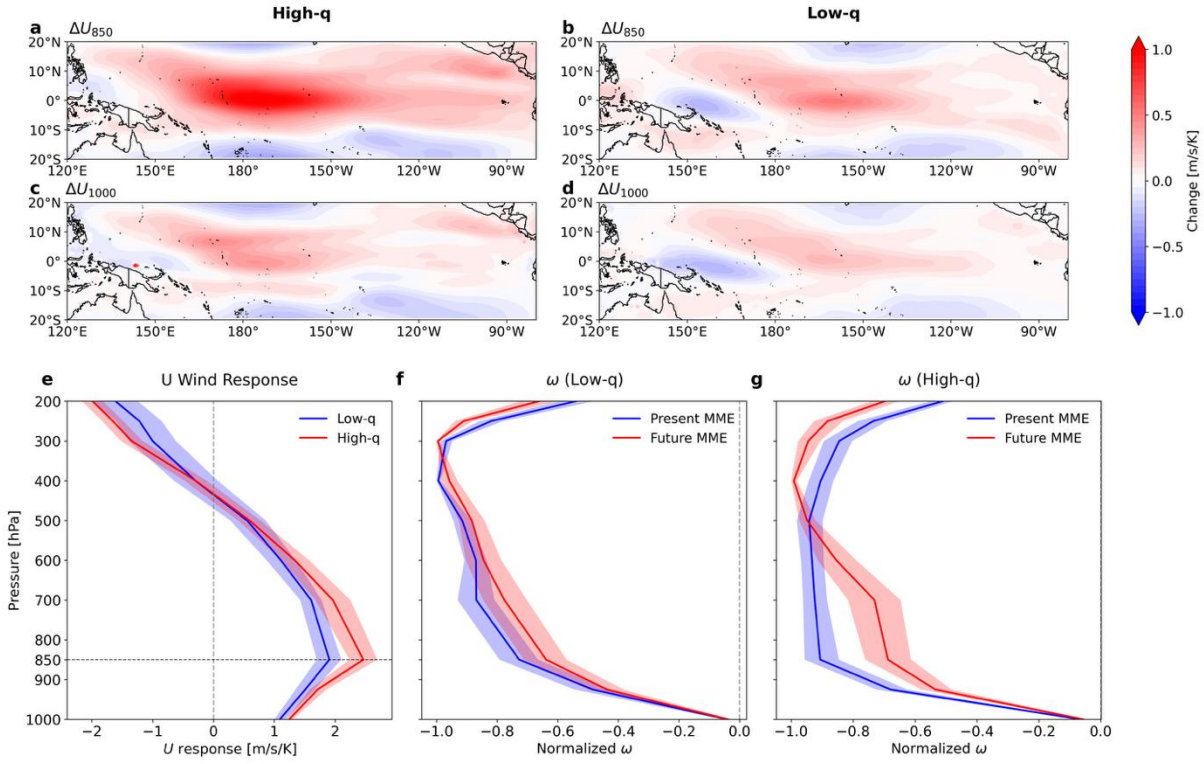
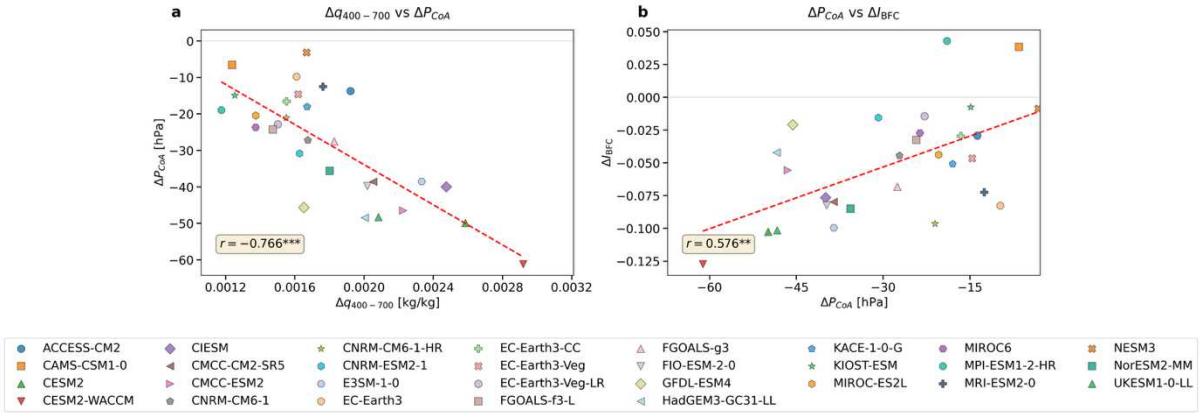


Figure 5. Comparison of El Niño zonal wind responses and vertical structures between model groups (High-q vs. Low-q) according to the magnitude of q change.

(a–d) Spatial distributions of projected changes in the ENSO-related zonal wind response (ΔU, m/s/K) at 850 and 1000 hPa for the group with large mid-tropospheric (400-700 hPa) q changes (High-q) and the group with small changes (Low-q). Panels (a) and (c) show the zonal wind responses at 850 hPa ($\mathbf{\Delta U_{850}}$) and 1000 hPa ($\mathbf{\Delta U_{1000}}$) for the High-q group, respectively, while (b) and (d) show the corresponding zonal wind responses for the Low-q group. The High-q group exhibits stronger intensification at 850 hPa than at 1000 hPa, consistent with a reduced projection of the lower-free-tropospheric wind response onto the boundary layer. (e) Vertical profiles of the ENSO-regressed zonal wind response over the Niño 4 region for the High-q and Low-q groups. The solid red (blue) line represents the ensemble mean of the High-q (Low-q) group, and the light shading indicates inter-model spread (95% bootstrap range). (f, g) Normalized omega response profiles over the Niño 4 region for the Low-q group (f) and High-q group (g). Blue and red lines denote the present-day and future climates, respectively. The High-q group exhibits a more pronounced upward displacement of the ascent profile than the Low-q group, consistent with a more top-heavy circulation structure. These composites indicate that stronger mid-tropospheric moistening is associated with an upward reorganization of ENSO-induced ascent and weaker coupling between the lower free troposphere and the boundary layer.



476

477 **Figure 6. Inter-model correlations among changes in mid-tropospheric specific humidity, convective center**

478 **altitude, and the BFC index**

479 (a) Scatter plot between the $\Delta \boldsymbol{q_{400-700}}$ and the change in the ascent-weighted mean pressure ($\Delta \boldsymbol{P_{CoA}}$, hPa). A

480 negative $\Delta \boldsymbol{P_{CoA}}$ indicates an upward displacement of the ascent centroid, where the center of the convective

481 response moves to higher altitudes. (b) Scatter plot between $\Delta \boldsymbol{P_{CoA}}$ and $\Delta \boldsymbol{I_{BFC}}$. Each marker in the scatter plots

482 represents an individual CMIP6 model, and the red dotted line is the linear regression line (***: p<0.001, **:

483 p<0.01).

484

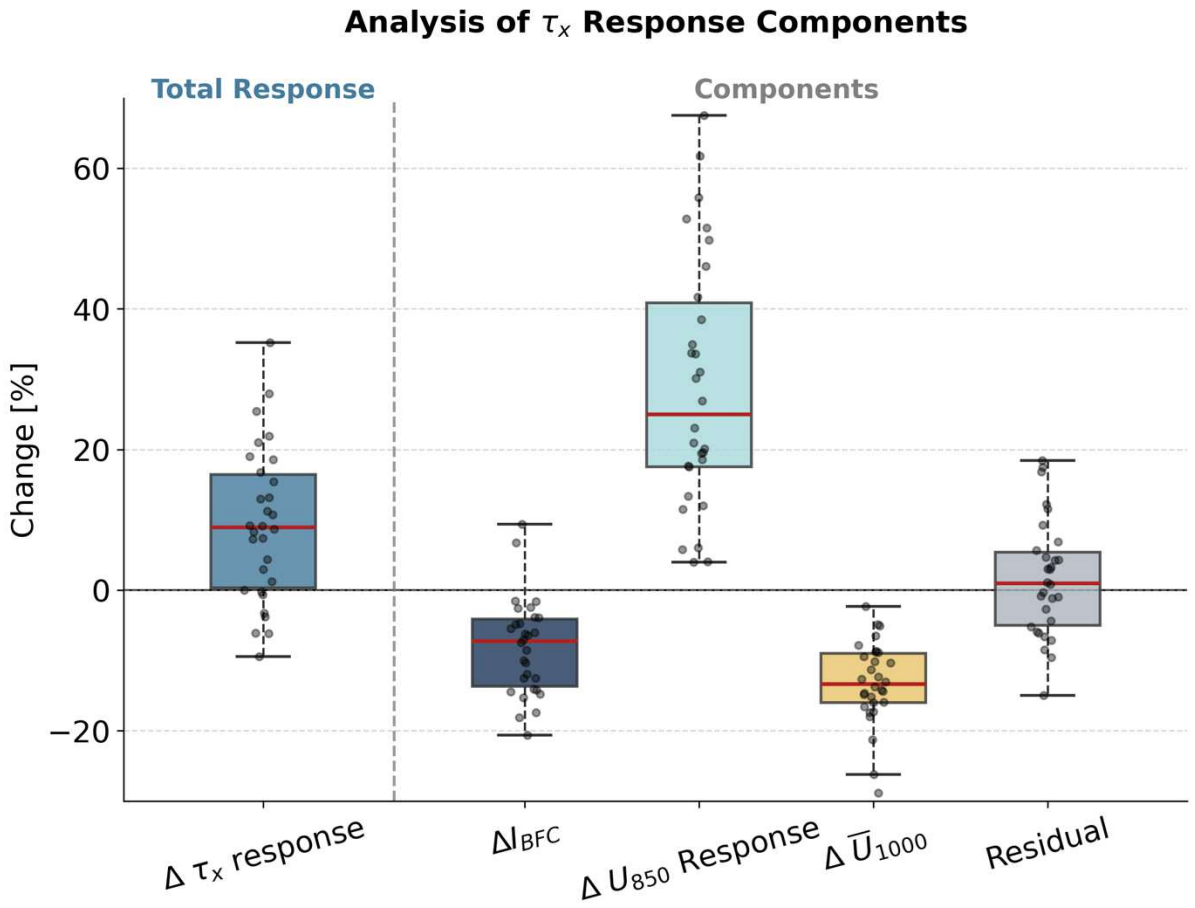


Figure 7. Physical decomposition of projected changes in the equatorial Pacific sea surface wind stress ($\boldsymbol{\tau_x}$) response.

A box plot showing the relative rate of change of the total $\boldsymbol{\Delta\tau_x}$ response and the contributions (Change, %) of its individual physical components. The total response is decomposed into the change in the lower-free-tropospheric zonal wind response ($\boldsymbol{\Delta U_{850}}$ Response), the lower-free-tropospheric and surface wind field decoupling effect (ΔBFC index), the change in the climatological mean background near-surface wind ($\boldsymbol{\Delta\bar{U}_{1000}}$), and a residual component that includes nonlinear effects. The horizontal red line within the box represents the median of the CMIP6 models, and the upper and lower boundaries of the box indicate the first and third quartiles (IQR). The semi-transparent gray dots overlaid on the boxes represent the distribution of the individual climate models used in the analysis. This quantitatively demonstrates that, although the lower-free-tropospheric zonal wind response ($\boldsymbol{\Delta U_{850}}$) is significantly amplified (a positive contribution) in a future climate, it is strongly offset (a negative contribution) by the wind field decoupling phenomenon (ΔBFC) and the weakening of the background mean wind field ($\boldsymbol{\Delta\bar{U}_{1000}}$).

References

1. McPhaden, M. J., Zebiak, S. E. & Glantz, M. H. ENSO as an Integrating Concept in Earth Science. *Science* **314**, 1740–1745 (2006).
2. Philander, S. G. H. El Niño Southern Oscillation phenomena. *Nature* **302**, 295–301 (1983).
3. Bjerknes, J. ATMOSPHERIC TELECONNECTIONS FROM THE EQUATORIAL PACIFIC. *Mon. Weather Rev.* **97**, 163–172 (1969).
4. Yeh, S. *et al.* ENSO Atmospheric Teleconnections and Their Response to Greenhouse Gas Forcing. *Rev. Geophys.* **56**, 185–206 (2018).
5. Ropelewski, C. F. & Halpert, M. S. Global and Regional Scale Precipitation Patterns Associated with the El Niño/Southern Oscillation. *Mon. Weather Rev.* **115**, 1606–1626 (1987).
6. Halpert, M. S. & Ropelewski, C. F. Surface Temperature Patterns Associated with the Southern Oscillation. *J. Clim.* **5**, 577–593 (1992).
7. Callahan, C. W. & Mankin, J. S. Persistent effect of El Niño on global economic growth.
8. Xue, A. *et al.* Super El Niño events drive climate regime shifts with enhanced risks under global warming. *Nat. Commun.* **16**, 11262 (2025).
9. Timmermann, A. *et al.* El Niño–Southern Oscillation complexity. *Nature* **559**, 535–545 (2018).
10. Collins, M. *et al.* The impact of global warming on the tropical Pacific Ocean and El Niño. *Nat. Geosci.* **3**, 391–397 (2010).
11. Cai, W. *et al.* Anthropogenic impacts on twentieth-century ENSO variability changes. *Nat. Rev. Earth Environ.* **4**, 407–418 (2023).
12. Kim, G.-I. *et al.* Deep ocean warming-induced El Niño changes. *Nat. Commun.* **15**,

522 6225 (2024).
523 13. Kim, S. T. *et al.* Response of El Niño sea surface temperature variability to greenhouse
524 warming. *Nat. Clim. Change* **4**, 786–790 (2014).
525 14. Beobide-Arsuaga, G., Bayr, T., Reintges, A. & Latif, M. Uncertainty of ENSO-
526 amplitude projections in CMIP5 and CMIP6 models. *Clim. Dyn.* **56**, 3875–3888 (2021).
527 15. Peng, Q., Xie, S.-P. & Deser, C. Collapsed upwelling projected to weaken ENSO under
528 sustained warming beyond the twenty-first century. *Nat. Clim. Change* **14**, 815–822 (2024).
529 16. Cai, W. *et al.* Increased variability of eastern Pacific El Niño under greenhouse
530 warming. *Nature* **564**, 201–206 (2018).
531 17. Cai, W. *et al.* Increased ENSO sea surface temperature variability under four IPCC
532 emission scenarios. *Nat. Clim. Change* **12**, 228–231 (2022).
533 18. Cai, W. *et al.* Changing El Niño–Southern Oscillation in a warming climate. *Nat. Rev.*
534 *Earth Environ.* **2**, 628–644 (2021).
535 19. Chen, L., Li, T., Yu, Y. & Behera, S. K. A possible explanation for the divergent
536 projection of ENSO amplitude change under global warming. *Clim. Dyn.* **49**, 3799–3811
537 (2017).
538 20. DiNezio, P. N. *et al.* Mean Climate Controls on the Simulated Response of ENSO to
539 Increasing Greenhouse Gases. *J. Clim.* **25**, 7399–7420 (2012).
540 21. Kim, S. T. & Jin, F.-F. An ENSO stability analysis. Part I: results from a hybrid coupled
541 model. *Clim. Dyn.* **36**, 1593–1607 (2011).
542 22. Kim, G.-I. & Kug, J.-S. Process-Based Analysis of El Niño–Southern Oscillation
543 Decadal Modulation. *J. Clim.* **35**, 4753–4769 (2022).
544 23. Bony, S. *et al.* How Well Do We Understand and Evaluate Climate Change Feedback
545 Processes? *J. Clim.* **19**, 3445–3482 (2006).

24. Held, I. M. & Soden, B. J. Robust Responses of the Hydrological Cycle to Global Warming. *J. Clim.* **19**, 5686–5699 (2006).

25. Bayr, T. & Latif, M. ENSO atmospheric feedbacks under global warming and their relation to mean-state changes. *Clim. Dyn.* **60**, 2613–2631 (2023).

26. Jin, F., Kim, S. T. & Bejarano, L. A coupled-stability index for ENSO. *Geophys. Res. Lett.* **33**, 2006GL027221 (2006).

27. Lindzen, R. S. & Nigam, S. On the Role of Sea Surface Temperature Gradients in Forcing Low-Level Winds and Convergence in the Tropics. *J. Atmos. Sci.* **44**, 2418–2436 (1987).

28. Small, R. J. *et al.* Air–sea interaction over ocean fronts and eddies. *Dyn. Atmos. Oceans* **45**, 274–319 (2008).

29. Charney, J. G. A Note on Large-Scale Motions in the Tropics. *J. Atmos. Sci.* **20**, 607–609 (1963).

30. Sobel, A. H., Nilsson, J. & Polvani, L. M. The Weak Temperature Gradient Approximation and Balanced Tropical Moisture Waves*. *J. Atmos. Sci.* **58**, 3650–3665 (2001).

31. Chien, M.-T. & Kim, D. Changes in stratiform heating structure due to surface warming weaken and accelerate convectively coupled Kelvin waves.

32. Sherwood, S. C. *et al.* Relative humidity changes in a warmer climate. *J. Geophys. Res. Atmos.* **115**, 2009JD012585 (2010).

33. Wright, J. S., Sobel, A. & Galewsky, J. Diagnosis of Zonal Mean Relative Humidity Changes in a Warmer Climate. *J. Clim.* **23**, 4556–4569 (2010).

34. Derbyshire, S. H. *et al.* Sensitivity of moist convection to environmental humidity. *Q. J. R. Meteorol. Soc.* **130**, 3055–3079 (2004).

570 35. Holloway, C. E. & Neelin, J. D. Moisture Vertical Structure, Column Water Vapor, and
571 Tropical Deep Convection. *J. Atmos. Sci.* **66**, 1665–1683 (2009).
572 36. Duan, S. Q., Ahmed, F. & Neelin, J. D. Moist heatwaves intensified by entrainment of
573 dry air that limits deep convection. *Nat. Geosci.* **17**, 837–844 (2024).
574 37. Schumacher, C., Houze, R. A. & Kraucunas, I. The Tropical Dynamical Response to
575 Latent Heating Estimates Derived from the TRMM Precipitation Radar. *J. Atmos. Sci.* **61**,
576 1341–1358 (2004).
577 38. Stachnik, J. P., Waliser, D. E., Majda, A. J., Stechmann, S. N. & Thual, S. Evaluating
578 MJO event initiation and decay in the skeleton model using an RMM-like index. *J. Geophys.*
579 *Res. Atmos.* **120**, (2015).
580 39. Back, L. E. & Bretherton, C. S. A Simple Model of Climatological Rainfall and
581 Vertical Motion Patterns over the Tropical Oceans. *J. Clim.* **22**, 6477–6497 (2009).
582 40. Back, L. E., Hansen, Z. & Handlos, Z. Estimating Vertical Motion Profile Top-
583 Heaviness: Reanalysis Compared to Satellite-Based Observations and Stratiform Rain
584 Fraction. *J. Atmos. Sci.* **74**, 855–864 (2017).
585

Supplementary Files

This is a list of supplementary files associated with this preprint. Click to download.

- Supplementary.pdf